Acta Oceanol. Sin., 2022, Vol. 41, No. 9, P. 137–148
https://doi.org/10.1007/s13131-022-1996-2
http://www.aosocean.com
E-mail: ocean2@hyxb.org.cn

Multisatellite observations of smaller mesoscale eddy generation in the Kuroshio Extension

Fangjie Yu[1, 2], Meiyu Wang[1], Sijia Qian[1], Ge Chen[1, 2*]

[1] College of Marine Technology, Faculty of Information Science and Engineering, Ocean University of China, Qingdao 266100, China

[2] Laboratory for Regional Oceanography and Numerical Modeling, Pilot National Laboratory for Marine Science and Technology (Qingdao), Qingdao 266237, China

Received 19 July 2021; accepted 13 December 2021

Abstract

Smaller mesoscale eddies (SMEs) have an important effect on the transmission of ocean temperatures, salinity, energy, and marine biochemical processes. However, traditional altimeters, the dominant sensors used to identify and track eddies, have made it challenging to observe SMEs accurately due to resolution limitations. Eddies drive local upwelling or downwelling, leaving signatures on sea surface temperatures (SSTs) and chlorophyll concentrations (Chls). SST can be observed by spaceborne infrared sensors, and Chl can be measured by ocean color remote sensing. Therefore, multisatellite observations provide an opportunity to obtain information to characterize SMEs. In this paper, an eddy detection algorithm based on SST and Chl images is proposed, which identifies eddies by characterizing the spatial and temporal distribution of SST and Chl data. The algorithm is applied to characterize and analyze SMEs in the Kuroshio Extension. Statistical results on their distribution and seasonal variability are shown, and the formation processes are preliminarily discussed. SMEs generation may be contributed by horizontal strain instability, the interaction of topographic obstacles and currents, and wind stress curl.

Key words: Kuroshio Extension, smaller mesoscale eddy, eddy detection algorithm, multisatellite remote sensing

Citation: Yu Fangjie, Wang Meiyu, Qian Sijia, Chen Ge. 2022. Multisatellite observations of smaller mesoscale eddy generation in the Kuroshio Extension. Acta Oceanologica Sinica, 41(9): 137–148, doi: 10.1007/s13131-022-1996-2

1 Introduction

Mesoscale eddies, as a ubiquitous phenomenon in the ocean, play a critical role in the transport of heat, salt, and nutrients in the ocean (Huang et al., 2012; Munk, 2001; Zhang et al., 2016). Studies have demonstrated that mesoscale eddies can lead to anomalous upward heat fluxes (Klein and Lapeyre, 2009; McWilliams et al., 2009; Su et al., 2018), control the nutrient budget, and enhance the primary production in the euphoric layer (Dandapat and Chakraborty, 2016; Zhang and Qiu, 2020). Microwave remote sensing is an essential means of ocean eddy detection, using altimeters to track and observe eddies. With the development of satellite observations, mesoscale eddies with horizontal scales above one hundred kilometers have been solved by traditional altimeters (Chen et al., 2020; Li et al., 2019b; Zhang et al., 2014). However, to date, only sea surface height (SSH) along the satellite orbits has been measured by nadir altimeters, and there are wide gaps between two tracks, which causes the altimeters to limit the spatial resolution of sea surface topography to exceed 100 km (Gaultier et al., 2016). Therefore, a significant part of the mesoscale dynamic process with a scale below 100 km is difficult to characterize by traditional altimeters (Durand et al., 2010; Trott et al., 2019). In the literature, eddies are named in terms of their dynamic or morphological properties. The baroclinic Rossby deformation radius is a dividing line for oceanographers to define mesoscale and submesoscale eddies (Alpers et al., 2013; Zhang et al., 2019a). However, it depends on latitude and oceanographic parameters, which do not have fixed values. Therefore, in this paper, we call eddies with scales below 100 km smaller mesoscale eddies (SMEs) according to the observation limitation of altimeters (Trott et al., 2019), although some literature called them submesoscale eddies (Fu and Le Traon, 2006). Based on the conclusion that mesoscale eddies with smaller sizes have a larger number (Zheng et al., 2015), there are abundant SMEs in the ocean, although altimeters do not accurately observe them. Observations of SMEs are helpful to understand the energy and material transfer from mesoscale eddies to submesoscale eddies and make up for the cognitive gaps in the limitation of traditional altimeters.

The application of satellite altimeters in the field of eddy observation is entering a platform stage. Infrared remote sensing and ocean color remote sensing have attracted much attention due to their advantages in smaller-scale observation. Eddies drive local water upwelling (cyclones) or downwelling (anticyclones) and leave signals on the SST field as cold (warm) features (Dong et al., 2011), which can be monitored by infrared remote sensing. SST maps with high spatial resolution are ideal for researching smaller mesoscale eddies (Gula et al., 2015; Qiu and Chen, 2005). Tedesco et al. (2019) proved that barotropic in-

Foundation item: The Marine S&T Fund of Shandong Province for Pilot National Laboratory for Marine Science and Technology (Qingdao) under contract Nos 2022QNLM050301-4 and 2021WHZZB1705; the National Natural Science Foundation of China under contract Nos 41527901 and 42030406; the National Key R&D Program of China under contract No. 2019YFD0901001.
*Corresponding author, E-mail: gechen@ouc.edu.cn

stability is a generation mechanism of smaller mesoscale eddies by using a numerical model and SST map; the generation process was marked by the transmission of kinetic energy from the mean flow to an eddy. Furthermore, sea surface temperature anomaly (SSTA) data can eliminate the effect of background flow in the sea surface on eddy detection. The study proves that the location of the SSTA is identical to sea surface height anomalies induced by eddies (Sun et al., 2016). To date, automatic algorithms based on SST images have been applied to observe and identify eddies (Dong et al., 2011). However, sea surface temperature (SST) is affected by solar radiation and heat exchange between the ocean and atmosphere, which is susceptible to the environment. Hence, the algorithm based on SST probably has noticeable noise. Ocean color remote sensing based on the principle of substance tracing provides a different view to observe and characterize SMEs. Eddies, which have a strong ability to carry and transport substances, not only cause SSH and SST anomalies but also lead to different chlorophyll concentrations (Chls) in the upper ocean. The linkage between mesoscale eddies and Chl *a* has been studied, cyclonic eddies might have a profound influence on the mesoscale variability in Chl *a* (Chelton et al., 2011; Shafeeque et al., 2021). Studies have found that upwelling caused by the vertical movement of cyclones can bring nutrients and increase biological productivity and chlorophyll concentration at the sea surface (McGillicuddy, 2016; Williams, 2011); conversely, anticyclones cause chlorophyll concentration to fall (Yang et al., 2020). In summary, SST and Chl anomalies are utilizable indicators to manifest the signal of smaller mesoscale eddies on the sea surface (Alpers et al., 2013; Zatsepin et al., 2019). The fusion of SSTA and Chl maps is a beneficial attempt to improve the reliability of eddy identification results by dual authentication.

In this paper, an eddy detection algorithm by fusing satellite infrared remote sensing and ocean color remote sensing was proposed to provide the possibility of SME observations. Subsequently, the algorithm was implemented in the Kuroshio Extension (KE, 28°–40°N, 138°–180°E) region. The KE is a strong eastward western boundary current extension formed by the Kuroshio separating from the coast of Japan (Qiu et al., 1991; Wang et al., 2020) and is recognized as an ocean current system with large amplitude meanders (Yasuda et al., 1992) (Fig. 1). The KE has the highest number of eddies of various scales in the North Pacific (Sasai et al., 2010). Eddy interactions are significant in modulating the decadal variability of the Kuroshio Extension System (Jia et al., 2019; Qiu and Chen, 2010) and affecting biogeochemical processes in the upper ocean (Uchiyama et al., 2017). Therefore, the KE is ideal for carrying out our algorithm. Recently, scientific discussions have shifted studies of mesoscale eddies to smaller mesoscale eddies, especially their generation. In the KE, Ji et al. (2018) characterized the spatial and temporal distribution of mesoscale eddies and suggested a role of horizontal shear instability in eddy generation based on Argo floats and ocean general circulation model for the Earth Simulation numerical model data. Luo et al. (2020) described that the smaller mesoscale flows on the edge of eddies have a close relationship with the frontal sharpening initiated by the mesoscale strain in the KE. Moreover, the spatial structure and temporal variation in vortices generated by the interaction between the Kuroshio and island obstacles were shown (Hsu et al., 2020; Isoguchi et al., 2009). However, these studies on smaller mesoscale eddies depend on numerical models or *in-situ* data, remote sensing observation of SMEs in the KE is needed.

The remainder of this paper is organized as follows. In Sections 2 and 3, a brief description of the data and method is given. Section 4 contributes to expressing the statistical results of SMEs from applying the algorithm in the KE. Simple spatial and temporal distributions and analyses of the generation of SMEs are carried out. Section 5 summarizes and discusses the method and results.

2 Data

2.1 *Sea surface temperature and sea surface temperature anomaly*

The SST data are an optimally interpolated SST daily product from January 1, 2011 to December 31, 2018, which utilizes microwave and infrared data (MW_IR) at a 9-km resolution. The data accuracy is in the range of 0.48–0.60°C (Li et al., 2021). Data are downloaded from the Remote Sensing Systems (REMSS) data archive (http://www.remss.com/).

The daily SSTA data are a multiscale ultra-high resolution (MUR) dataset created and published by National Oceanic and Atmospheric Administration Environment Research Division (NOAA ERD) based on Jet Propulsion Laboratory (JPL) MUR climatology (2003–2014) and SST data. The root mean square error of the SST data is less than 0.1°C (Abhishek and Sil, 2019). This product combined multiple sensors, including Advanced Microwave Scanning Radiometer-EOS, Advanced Very High Resolution Radiometer, Moderate Resolution Imaging Spetroradiometer, Special Sensor Microwave Imager, Visible and Infrared Imager/Radiometer Suite (VIIRS), and *in-situ*. The JPL provides the ultrahigh-resolution of 1 km under the support of

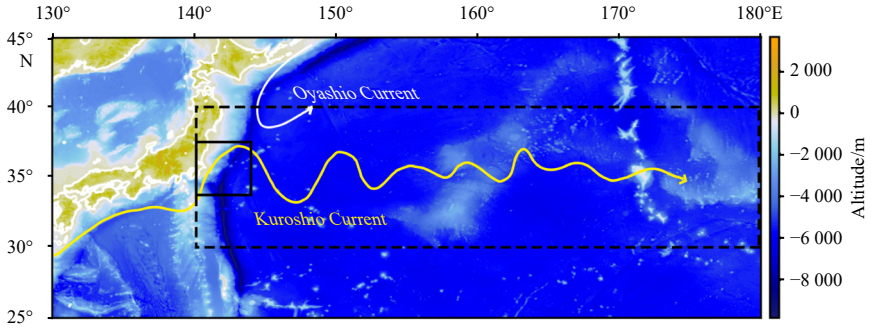

Fig. 1. Geographic distribution of the main currents in the Kuroshio Extension (area bounded by a dashed line), the yellow line represents the Kuroshio Current spindle, and the white line represents Oyashio Current. The solid black box is the eddy high incidence area mentioned below. The base map shows the bathymetry data from General Bathymetric Chart of the Oceans (https://www.gebco.net/data_and_products/gridded_bathymetry_data/).

National Aeronautics and Space Administration (NASA) Making Earth Science Data Records. The data from 2014 to 2015 are downloaded from the Environmental Research Divison's Data Access Program (https://coastwatch.pfeg.noaa.gov/erddap/).

The two types of SST data are used to improve the efficiency of the algorithm proposed in this study and save computing resources. The SST data from REMSS are used to identify and locate SMEs in the entire KE area, and the SSTA data from NOAA with the ultra-high resolution are used to further identify and observe eddies accurately in a small area.

2.2 *Satellite chlorophyll a concentration data*

The VIIRS level 3 daily data on chlorophyll *a* concentration with a 4-km resolution from January 1, 2011 to December 31, 2018, are downloaded from the OceanColor web (https://oceancolor.gsfc.nasa.gov/). The data are processed by the NASA Goddard Space Flight Center Ocean Biology Processing Group and are calculated by the ocean color index algorithm (Hu et al., 2012). The data are used to characterize the vertical nutrient transport in smaller mesoscale eddies.

2.3 *Satellite altimetry data*

Satellite altimetry data derived from a global delayed-time L4 product are provided by the Copernicus Marine Environment Monitoring Service (CMEMS, https://marine.copernicus.eu/). This product is processed by the Ssalto multimission ground segment/Data Unification and Altimeter Combination System multimission altimeter data processing system. The gridded sea level anomaly (SLA) data with high resolution (1/4)°×(1/4)° merge the L4 product from the different altimeter missions available and make an optimal interpolation, whose precision can reach the centimeter-level (Taburet et al., 2019). The SLA and absolute geostrophic velocities (zonal component (ugos) and meridian component (vgos) derived from absolute dynamic topography) are used to characterize mesoscale eddies and geostrophic currents.

2.4 *Wind stress curl data*

NOAA CoastWatch distributes neal-time wind stress curl data with a 0.25-degree resolution. The data begin with wind velocity measurements from the Advanced Scatterometer (ASCAT) aboard the European Organization for the Exploitation of Meteorological Satellites METOP-A satellite. ASCAT is a microwave scatterometer designed to measure surface winds over the global ocean. NOAA CoastWatch processes wind velocity to wind stress and wind stress curl. The information regarding data can be found at NOAA/National Environmental Satellite, Data, and Information Service (http://manati.orbit.nesdis.noaa.gov).

2.5 *Satellite-tracked drifting buoy data*

Global Drifter Program quality-controlled 6-hourly interpolated data are conducted by the Drifter Data Assembly Center (DAC) at the Atlantic Oceanographic and Meteorological Laboratory from ocean surface drifting buoys (Hansen and Poulain, 1996). The dataset includes SST and current data collected by satellite-tracked surface driftering buoys for the NOAA Global Drifter Program. DAC applies quality control procedures to edit these data and interpolates them using an optimum interpolation procedure: kinging. The drifter data are downloaded from the internet (https://www.aoml.noaa.gov/phod/gdp/interpolated/data/all.php).

3 Methods

Eddy can be defined as the rotational motion of the fluid mass, in which the velocity field is represented as a rotating flow. The rotating direction of the velocity vector can be clockwise or counterclockwise. SST data can be convoluted with the Sobel operator to obtain the thermal-wind velocity (V) for eddy detection. And, the vertical movement of SMEs contributes to variations in chlorophyll concentrations. Thus, based on the effect of eddies on SSTAs and chlorophyll *a* concentrations, a fusion algorithm incorporating Chl based on SST is used to identify SMEs. The basic idea of the algorithm is to extract eddy features from SST and Chl images respectively, and then detect eddies both in information derived from SST and Chl data.

There are four main steps: (1) data preprocessing; (2) eddy feature extraction; (3) tracking; (4) credibility assessment (Fig. 2).

Step 1: data preprocessing. The SSTA data are calculated by original SST grid data from REMSS (SSTA=SST– SST_{avg}; SST_{avg} is the daily climate average of the SST, which is calculated by the daily SST data from January 1, 2011 to December 31, 2018). Gaussian smoothing is used to smooth SSTA and Chl data for reducing the noise of the original images. A Sobel gradient operator is then implemented to convolute SSTA data to obtain the thermal-wind velocity. The operation uses two 3×3 kernels to compute approximations of spatial derivatives ($\boldsymbol{G}_y$ and $\boldsymbol{G}_x$) of SSTA and Chl:

$$\boldsymbol{G}_y = \begin{bmatrix} 1 & 2 & 1 \\ 0 & 0 & 0 \\ -1 & -2 & -1 \end{bmatrix} * \boldsymbol{A}, \quad \boldsymbol{G}_x = \begin{bmatrix} 1 & 0 & -1 \\ 2 & 0 & -2 \\ 1 & 0 & -1 \end{bmatrix} * \boldsymbol{A}, \tag{1}$$

where x and y are the coordinate axes for space and correspond to the measurements to the east and north, respectively; * represents the 2-D convolution operation; $\boldsymbol{A}$ means the matrix extracted from the SSTA and Chl grid data; $\boldsymbol{G}_x$ and $\boldsymbol{G}_y$ represent two approximations of the zonal and meridional derivatives for each point, respectively ($\boldsymbol{G}_{x\text{-ssta}}$ and $\boldsymbol{G}_{y\text{-ssta}}$ derived from SSTA images,

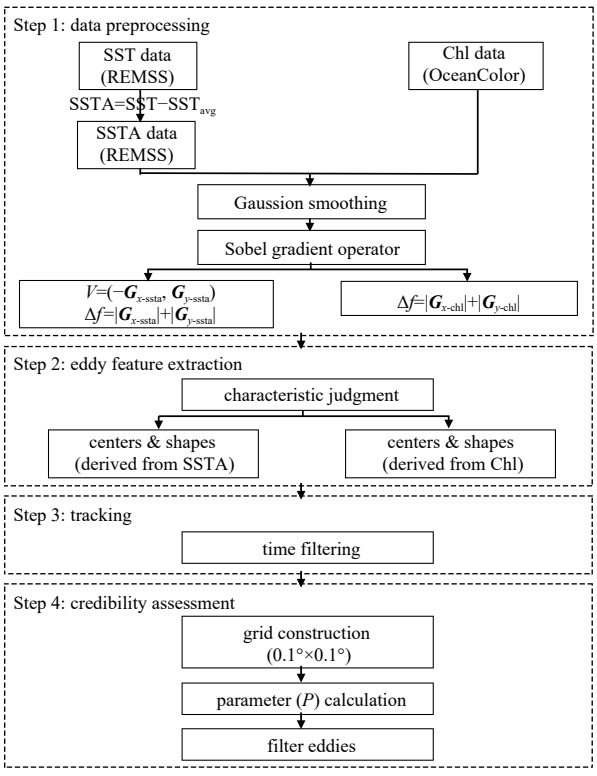

Fig. 2. Algorithm flow chart of eddy detection based on sea surface temperature (SST) and chlorophyll concentration (Chl) data.

$\boldsymbol{G}_{x\text{-chl}}$ and $\boldsymbol{G}_{y\text{-chl}}$ derived from Chl images).

The thermal-wind velocity is obtained by the vector corresponding to the baroclinic velocity component contributed by the temperature based on the thermal-wind relationship and the first-order (linear) water state equation (Dong et al., 2011). To ensure that V has the correct rotating direction on both hemispheres, the V derived from SSTA images is defined as $(-\boldsymbol{G}_{x\text{-ssta}}, \boldsymbol{G}_{y\text{-ssta}})$ in the Northern Hemisphere and $(\boldsymbol{G}_{x\text{-ssta}}, \boldsymbol{G}_{y\text{-ssta}})$ in the Southern hemisphere. The gradient amplitude Δf was calculated by

$$|\Delta f| \approx |\boldsymbol{G}_x| + |\boldsymbol{G}_y| . \tag{2}$$

Step 2: eddy feature extraction. Nencioli et al. (2010) proposed a vector-geometry eddy detection algorithm that can identify eddies from any velocity field because it is entirely based on the geometry of the flow field. Dong et al. (2011) applied this scheme to detect eddies based on thermal-wind velocity derived from SST data in the KE region. Referring to the vector-geometry algorithm, we fused the judgment of SST and Chl abnormal areas to identify SMEs, which characterized eddies by the following conditions.

Check each grid point for detecting eddy centers: (1) the eddy center is the local maximum (anticyclone) or minimum (cyclone) in a 5×5 neighborhood grid on the SSTA and Chl gradient amplitude; (2) around the eddy center, the direction of V has to change with a constant sense of rotation, and the components of V have to reverse in sign across the eddy center along with the zonal and meridional directions.

Detect eddy shapes once eddy centers are determined: (1) the eddy shape is the maximum gradient amplitude contour around the eddy center on the SSTA and Chl maps; (2) the SSTA and Chl gradient values gradually increase from the eddy center to the eddy shape. Cyclones manifest closed-contour negative SSTA, anticlockwise rotation, and positive Chl. Anticyclones manifest closed-contour positive SSTA and clockwise rotation.

The eddy features satisfying the above conditions are extracted from SST and Chl data respectively. Figure 3 shows examples of the V derived for a cold and a warm SME in the KE, which indicates how eddies are identified from SSTA. Figure 4 shows an example of SME identification from SST and Chl data over a wide area (28°–40°N, 138°–160°E). It can be seen that the algorithm is feasible to identify eddies by extracting SSTA and chlorophyll concentration anomaly. Moreover, Chl data with high spatial resolution help to identify smaller-scale eddies ignored by SST to some extent.

Step 3: tracking. An eddy tracking algorithm proposed by Dong et al. (2011) is used to track eddies. In summary, eddy tracks are determined by comparing the centers of the same type at successive time steps. The track of an eddy is updated by searching for eddy centers at time t+1 within a searching area of N×N grid points centered around the eddy location at time t. To avoid dividing a successive track into multiple tracks, eddies cannot be captured outside the searching area from time t to time t+1. Depending on the spatial and temporal resolution of the dataset, as well as the characteristics of the mean flow field, the size of the searching area is determined. Because the moving

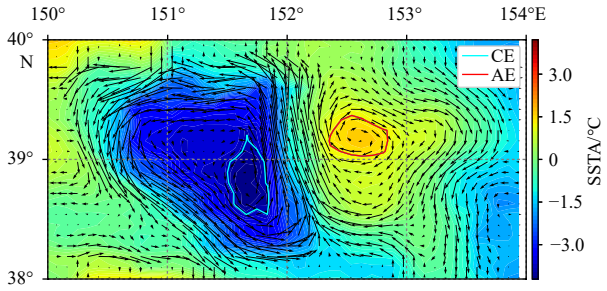

Fig. 3. Examples of cyclonic eddy (CE) and anticyclonic eddy (AE). Vectors are thermal-wind velocities, and the color is sea surface temperature anomaly (SSTA) from the Remote Sensing Systems. The solid lines are eddy boundaries.

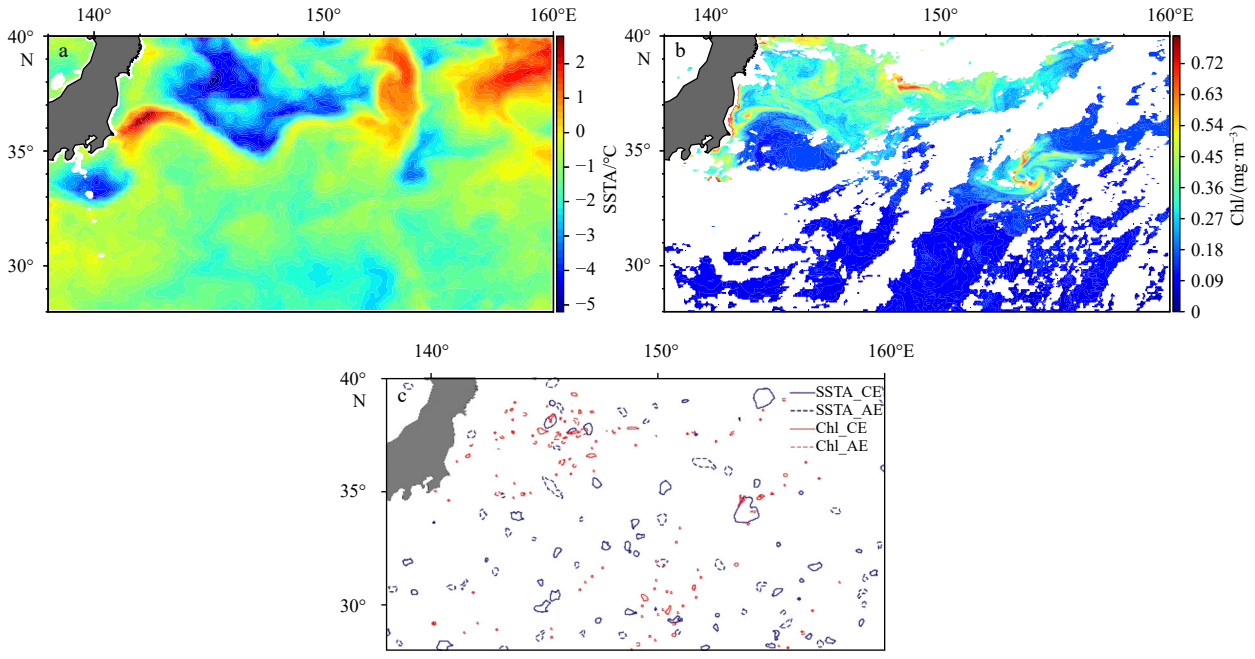

Fig. 4. An example of eddy identification from sea surface temperature (SST) and chlorophyll concentration (Chl) maps. a. Sea surface temperature anomaly (SSTA) map; b. Chl map; c. eddy shapes extracted from SSTA and Chl maps.

speed of eddies that are advected by the local flow is approximately on a scale of 10 cm/s and the temporal sampling frequency of our data is daily, the search radius is built as 15 km (Dong et al., 2011).

According to the tracking algorithm, the lifetime of eddies can be obtained. Considering the SST data are easily affected by complicated signals from the environment, we filter out eddies with lifetimes less than two days to reduce the impact of SST variability resulting from uncertain factors.

Step 4: credibility assessment. To obtain more accurate detection results, a parameter (P) was established to measure anomalies on a time scale, comparing the anomalies recorded in given months over the years (2011–2018). The higher the value, the more reliable the result is.

To calculate the parameter, a 0.1°×0.1° grids is first built, where grid dots within eddy shapes derived from SST or Chl are marked as 1, eddy shapes derived both from SST and Chl are marked as 2, and those without eddy shapes are marked as 0 (Figs 5a, b). The parameter(P) calculated at grid dots is defined as follows:

$$P_{(i,j)} = \begin{cases} \alpha P_{\mathrm{SSTA}(i,j)} + \beta P_{\mathrm{Chl}(i,j)} \ (\alpha+\beta=1, (i,j)=2), \\ P_{\mathrm{SSTA}(i,j)} \text{ or } P_{\mathrm{Chl}(i,j)} \ ((i,j)=1), \end{cases} \tag{3}$$

where i, j represent the row and column number of grids, respectively; $P_{(i,j)}$ is the probability that there is an eddy at pixel (i, j); $P_{\mathrm{SSTA}(i,j)}$ and $P_{\mathrm{Chl}(i,j)}$ are the probabilities calculated based on the SSTA and Chl maps. The $P_{\mathrm{Chl}(i,j)}$ is calculated by the following equations,

$$\mathrm{Chl}_{\mathrm{s}(i,j)} = \sum_{m=1}^{y}\sum_{n=1}^{d}\mathrm{Chl}_{(i,j)} \ (m=1,2,\ldots,y; n=1,2,\ldots,d), \tag{4}$$

$$\overline{\mathrm{Chl}_{\mathrm{s}(i,j)}} = \mathrm{Chl}_{\mathrm{s}(i,j)}/y \cdot d, \tag{5}$$

$$P_{\mathrm{Chl}(i,j)} = \frac{|\mathrm{Chl}_{\mathrm{d}(i,j)} - \overline{\mathrm{Chl}_{\mathrm{s}(i,j)}}|}{\mathrm{MAX}(|\mathrm{Chl}_{(i,j)} - \overline{\mathrm{Chl}_{\mathrm{s}(i,j)}}|)}, \tag{6}$$

where $\mathrm{Chl}_{\mathrm{s}(i,j)}$ represents the sum of chlorophyll concentration value ($\mathrm{Chl}_{(i,j)}$) dataset from the chlorophyll value of the month over the years in pixel (i, j) (y equals the number of years that we use to calculate the monthly average Chl and d equals the number of days in the month); $\overline{\mathrm{Chl}_{\mathrm{s}(i,j)}}$ represents the monthly average of $\mathrm{Chl}_{\mathrm{s}(i,j)}$ over the years; and $\mathrm{Chl}_{\mathrm{d}(i,j)}$ is the chlorophyll value on the day that the eddy is identified. Similarly, $P_{\mathrm{SSTA}(i,j)}$ is calculated by the same formula.

α and β represent the empirical weight coefficients of SSTA and Chl for the eddy, respectively. There is a significant correction (approximately 0.5–0.7) between the mesoscale variability of Chl and SST and the influence of eddies (Shafeeque et al., 2021). The accuracy of the algorithm based on the SSTA is discussed by comparison with a 10-year global mesoscale eddy dataset based on SLA in the KE. The results indicated that true eddies account for more than 70% of the total number of detected eddies (Qian et al., 2021). For these reasons, the empirical value α is set to 0.7, and β is 0.3 in the KE accordingly. The two parameters give flexibility to the algorithm, which can be adjusted appropriately.

The algorithm filters eddies by detecting the P-value both in the eddy shapes derived from SST and Chl. Theoretically, the higher the P-value is, the more likely the detected result is an eddy and the more accurate the algorithm. To objectively assess the algorithm accuracy, a validation area (28°–33°N, 148°–153°E) is built. SMEs with different values of P are evaluated on a random basis for 12 days (one day per month) in the area. For these days, detection accuracy (DA) is defined as the number of true eddies (Nt) detected by the algorithm divided by the total number of eddies (N). True eddies are manually detected according to the eddy definition as a selection criterion. Table 1 shows the DA results in the 12 maps selected for validation. Accordingly, a high DA value (90%; P≈0.7) is selected to obtain a credible result. As long as there is one point in the eddy where P-value satisfies the condition, the eddy will be taken as the final result (Fig. 5d). The

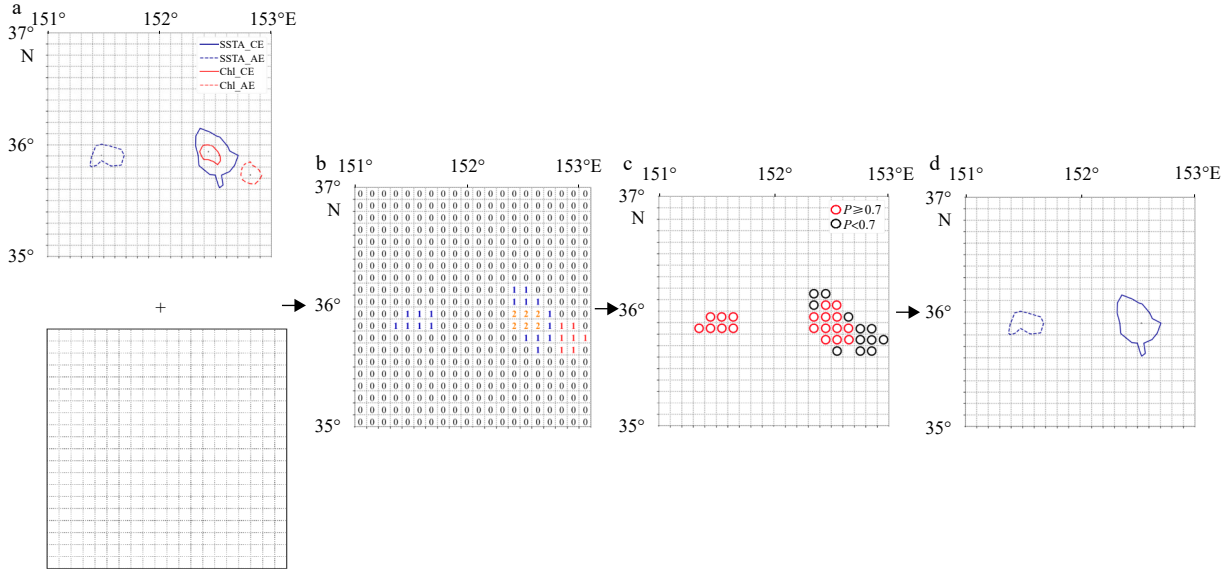

Fig. 5. Flow chart of credibility assessment expresses how to detect eddy both in the extracted shapes from sea surface temperature (SST) and chlorophyll concentration (Chl). a. The extracted eddy features, AE means anticyclonic eddy, CE means cyclonic eddy; b. the marked grid, whose color is meaningless; c. the result after parameter calculation, red circles mean the grids satisfy conditions, black circles are the opposite; d. the final results.

Table 1. Algorithm results for the 12 days are used for valuation

Parameters	Value								
P	0.1	0.2	0.3	0.4	0.5	0.6	0.7	0.8	0.9
N	139	116	92	72	50	38	25	18	8
Nt	75	61	49	42	34	28	23	17	8
DA	53.96%	52.59%	53.26%	58.33%	68.00%	73.68%	92.00%	94.44%	100%

Note: *N* is the total number of eddies detected by the algorithm; Nt is the number of true eddies identified by manual detection; DA is the detection accuracy of the algorithm.

information (shapes and centers) of eddies is mainly determined by the SST when there is a spatial divergence between SST and Chl.

According to the detection algorithm, SMEs were detected, including their centers, shapes, types, sizes, and lifetimes. The size of SME is defined as the radius of the circle that has the same area as the region with the shape.

4 Results

4.1 *Temporal and spatial distribution of smaller mesoscale eddies*

In general, the Eulerian method and Lagrangian method serve to count eddies. The Eulerian method is used to determine how many eddies exist at each moment. The Lagrangian method is employed when information about eddy generation is required (Ji et al., 2018). According to the Lagrangian method, a total of 1904 smaller mesoscale eddy tracks are identified from a characteristic dataset from 2014. More than half are identified as cold eddies (1 041; 54.67%), and the rest as warm eddies (863; 45.33%). With the Eulerian method, the total number of eddies is 7 388, which includes cyclonic eddies (4 070, 55.09%) and anticyclonic eddies (3 318, 44.91%).

Figure 6a shows the histograms of SME diameters using the Eulerian method. The number decreases with increasing diameter, which is consistent with the conclusion that eddies with smaller sizes have a larger number. The variation trend is similar between cyclonic eddies and anticyclonic eddies, and the peak value of both is approximately 30–40 km. The peak is close to the first baroclinic deformation radius. Figure 6b shows the seasonal distribution of SMEs. Cyclonic eddies peak in February, and anticyclonic eddies peak in December. Overall, there is an obvious seasonal variation in SMEs, with more eddies (2 509) encountered in winter (December–February) and fewer eddies (1 821) encountered in summer (June–August), which might be affected by frontal/mixed-layer instability. The result coincides with Sasaki et al. (2014), frontal instability set up by large-scale atmospheric forcing in winter contributes to a significant seasonal modulation. Figure 7 plots the spatial distribution of the number of SMEs in 0.5°×0.5° bins. It shows that the distribution of anticyclonic eddies is relatively even within the KE and that cyclonic eddies are more frequently encountered north of 34°N. In addition, anticyclonic eddies are located more downstream of the KE than upstream, with more births in spring. The baroclinic instability might provide the primary energy source for the regional seasonal eddy variability, which was demonstrated by Yang and San Liang (2018). According to the latitude, we divide the KE region into three parts. In the northern part (36°–40°N), the number of SMEs accounts for 37.7% of the total, 28.7% in the middle part (32°–36°N, where the main axis of the Kuroshio Current (KC) is located) and 33.6% in the southern part (28°–32°N). Combined with the geographic distribution of the KE (Fig. 1), SMEs are more distributed on both sides of the KC spindle, where dynamic processes are intense and there are abundant mesoscale eddies, and the KC tends to generate cyclonic eddies in the northern part (Fig. 7b). For example, more cyclonic eddies are located north of the strong KC (Fig. 7b black box), which are possibly caused by the flow instability after the current hit the Japanese coast or horizontal strain instability of the strong current.

4.2 *SME formation at the periphery of mesoscale eddies*

SMEs often occur where horizontal strain instability occurs, especially at the periphery of mesoscale eddies (Li et al., 2019a; Zatsepin et al., 2019; Zhang et al., 2020). The mesoscale eddy, the ocean dynamic phenomenon with the largest kinetic energy, can cause an uneven distribution of the horizontal shear strain rate (S) field and energize the SME on the sea surface (Capet et al., 2008). When the horizontal stain is strong, it favors highly smaller mesoscale motions (Zhang and Qiu, 2018). SMEs gradually dissipate the energy and nutrients of mesoscale eddies with the evolution and development of mesoscale eddies.

The formation and evolutionary progress of an eddy that existed from May 10 to 22, 2014, is presented in Figs 8 and 9. SSTA and SLA maps depict the evolution of SST and sea level anomalies in the eddy region, respectively (Fig. 8). Figures 8a and e show a cold temperature anomaly that appeared on the sea surface at the contour of a mesoscale eddy bulge. With time, the signature of temperature became more pronounced, and the cold temperature anomaly gradually formed the shape of an eddy

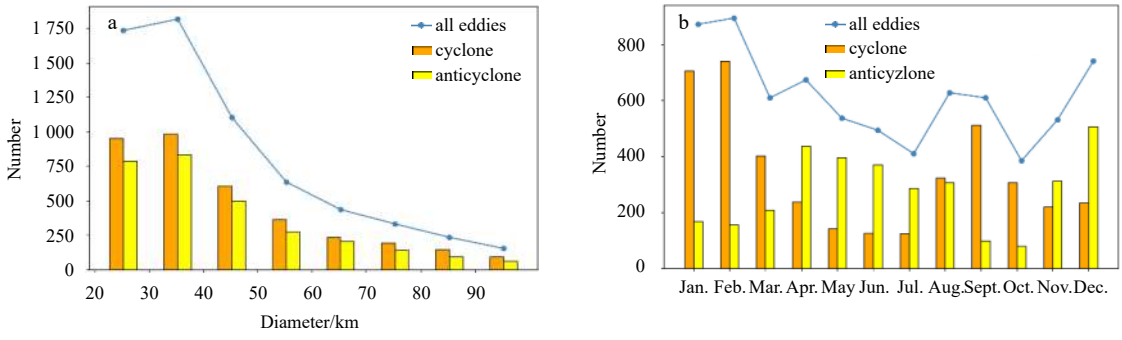

Fig. 6. Histograms of eddy diameter (a) and seasonal distribution (b) in the number of smaller mesoscale eddies.

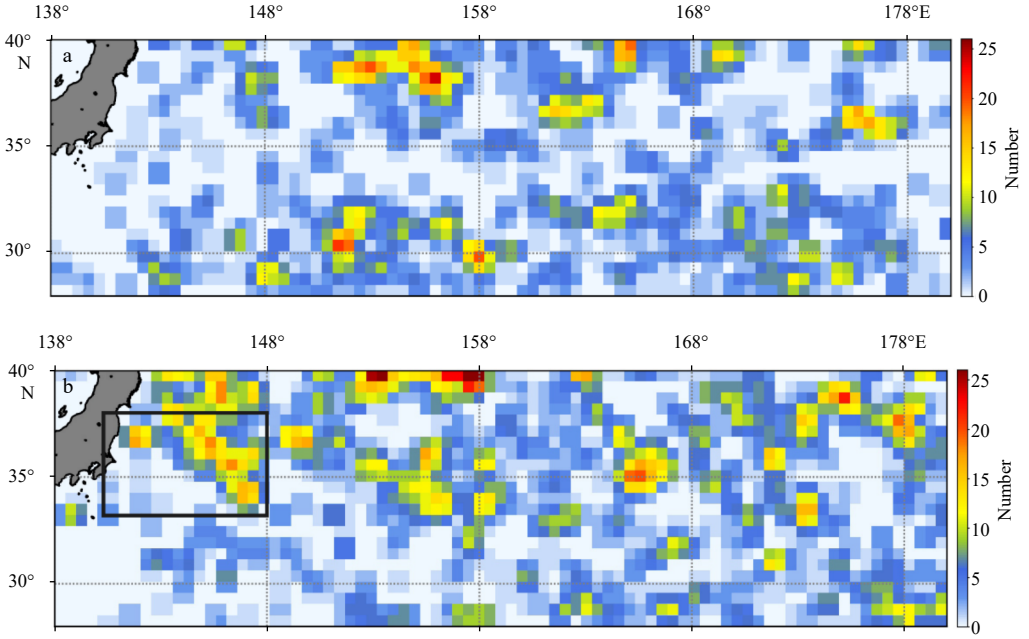

Fig. 7. Spatial distribution of the number of identified smaller mesoscale eddies in the Kuroshio Extension region: anticyclonic eddies (a) and cyclonic eddies (b). The bin size is 0.5°×0.5°. The black box marks an area with dense cyclonic eddies.

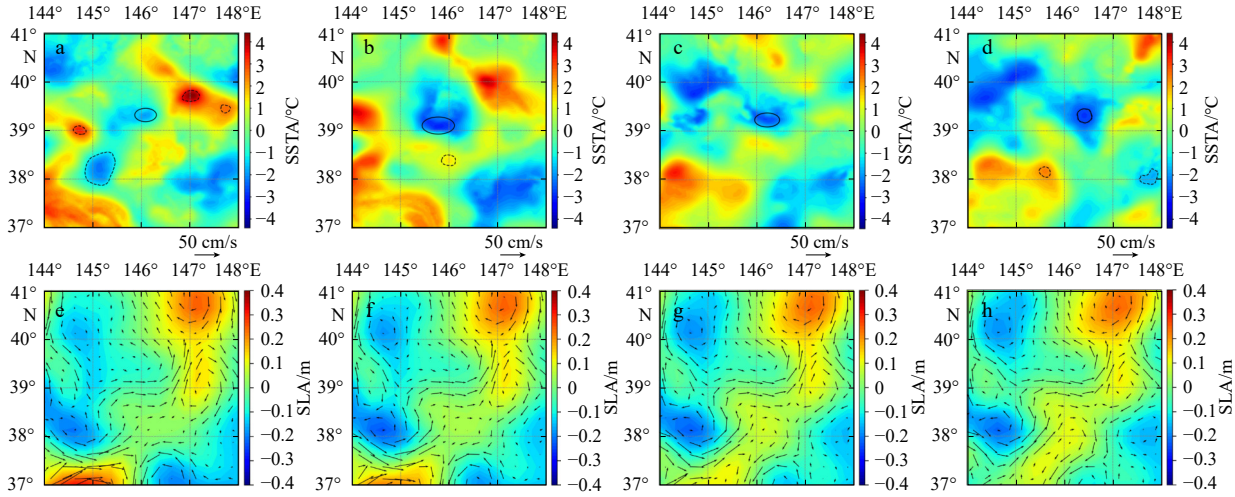

Fig. 8. Upper panels: sea surface temperature anomaly (SSTA) field from NOAA on May 8 (a), May 11 (b), May 14 (c), May 16, 2014 (d), respectively. Lower panels: sea level anomaly (SLA) field (colors) superimposed current velocity field (black arrows) on the same date with upper panels (e–h). The black circles mark the locations of smaller mesoscale eddies identified by SSTA from NOAA. The solid one is the example observed above.

(Fig. 8d, solid circle, 39.3°N, 146.4°E). During its formation, the SSTA signature moved eastward and gradually broke out of the range of the mesoscale eddy. The eddy diameter varied between 28 km and 50 km, and the maximum temperature difference between the core and edge of the cold eddy was approximately 1.8°C. SMEs have a dynamic movement that moves violently in a vertical direction. At the beginning of their existence, the vertical transfer of nutrients can occur as they form in regions with strongly sloping density surfaces (Alpers et al., 2013), which can transport Chl from the lower layers to the sea surface. Figure 9b shows a significantly high value of Chl in the eddy region, which coincided with the SST signature. The chlorophyll concentration in the center of the eddy was approximately 0.3 mg/m^3 higher than that in its margin, which is presumably caused by the vertical transmission of the eddy. It is worth noting that there was a flow trajectory of chlorophyll from the mesoscale eddy to the smaller mesoscale eddy (Fig. 9a), which indicates that mesoscale eddy has a relationship with the SME generation.

During the eddy lifetime, a surface drifter moving with the eddy was captured, and its trajectory is depicted in Fig. 10, and the corresponding parameters extracted from the time series are plotted in Fig. 10C. The process is divided into four parts. At the initial stage, the drifter was located at the periphery of a mesoscale eddy and moved eastward, with a velocity of approximately 40 cm/s. Until May 15, 2014, the drifter moved out from the edge of the mesoscale eddy and moved into the center of the smaller mesoscale eddy, whose velocity decreased to approximately 10 m/s (Figs 10C a, b). After approximately one day and a half, the drifter rapidly moved away from the core of the eddy, reversed direction toward the west, and rotated anticlockwise

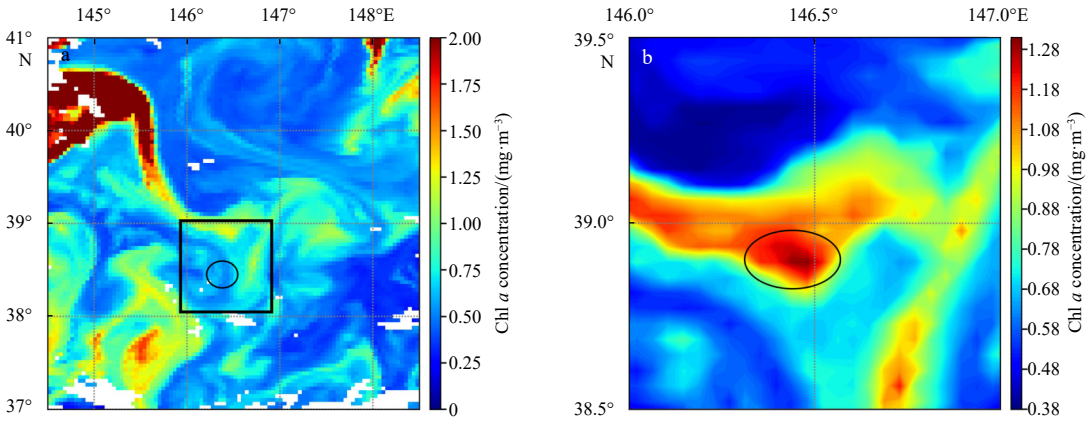

Fig. 9. Observed chlorophyll *a* concentration snapshots on May 19, 2014: the snapshot of observed the smaller mesoscale eddy (a); an enlarged portion of the black box in Fig. 8a (b). The black circles mark the position of the eddy.

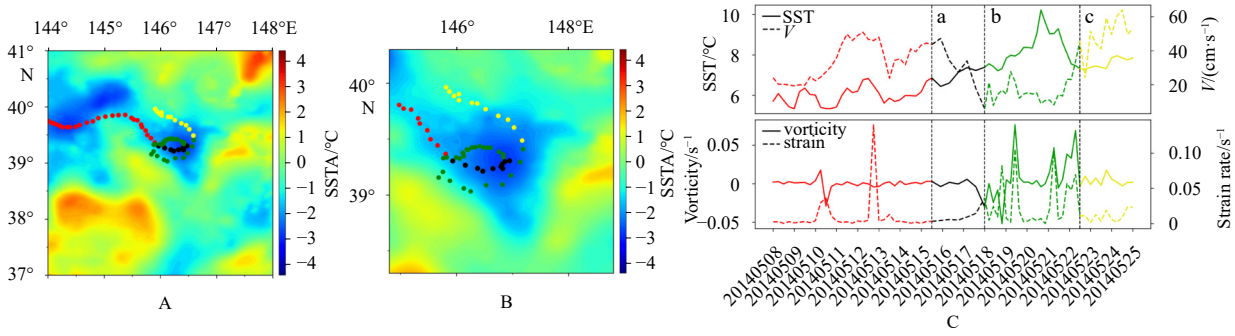

Fig. 10. The trajectory information of drifter: the snapshot of sea surface temperature anomaly (SSTA) on May 16, 2014, superimposed sample points of drifter from May 8, 2014 to May 25, 2014, at a 6-h time interval (A); the color of points represents four parts of trajectory; the snapshot of SSTA superimposed sample points of drifter from May 13, 2014 to May 25, 2014, shown as an enlarged portion of A (B), calculated properties of the drifter, including sea surface temperature (SST) and velocity (*V*) (upper panels), vorticity and strain rate (lower panels) (C). The dashed lines (a, b, c) marked the times for the drifter to enter the eddy, leave the eddy center, and leave the eddy, respectively.

along the periphery of the eddy from May 18 to 23, 2014 (Figs 10C b, c), which corresponded to the cyclone in the Northern Hemisphere. At this stage, the velocity value of the drifter maintained a relatively stable low value (approximately 15 cm/s). Afterward, the drifter moved out of the smaller mesoscale eddy at high speed. According to the change in temperature, the temperature decreased slightly when the drifter entered the eddy center (Figs 10C a, b) and increased when the drifter left the center and moved around the edge of the eddy (Figs 10C b, c). The temperature difference between the center and edge of the smaller mesoscale eddy was coincident with the features of a cyclone. In addition, Fig. 10C shows the variation in the relative vorticity (ζ) and shear strain rate (S) derived by the drifter. ζ is the relative vorticity, which is a measure of the tendency for fluid to rotate. The strain flow field is characterized by stretching along one direction and squeezing along the perpendicular direction. S can demonstrate the deformation rate of the geostrophic fluid field (Zhang et al., 2019b). The parameters are calculated by

$$S = \sqrt{\left(\frac{\partial u}{\partial x} - \frac{\partial v}{\partial y}\right)^2 + \left(\frac{\partial v}{\partial x} + \frac{\partial u}{\partial y}\right)^2}, \tag{7}$$

$$\zeta = \frac{\partial v}{\partial x} - \frac{\partial u}{\partial y}, \tag{8}$$

where x and y are the coordinate axes for space and correspond to the measurements to the east and north, respectively; the variables u and v are zonal and meridional components of velocity, respectively.

The sea surface horizontal strain increased after the drifter moved into the eddy, which indicates sea surface current instability. Similarly, the vorticity changed significantly with the increasing horizontal strain rate. When the drifter moved along the edge of the eddy, the positive vorticity coincided with the features of the cyclone (Figs 10C b, c), except for the negative value on May 18. The abnormal vorticity was possibly affected by unsteady motion in the center of the eddy. The drifter trajectory and the variety of these properties suggest that the formation of the SME has a relationship with the horizontal strain instability. The direction of flow and the distribution of Chl also show the material transfer from mesoscale eddies to smaller mesoscale eddies.

4.3 *Eddy formation on the topographic obstacles*

The interaction of topographic obstacles and currents is an important factor for the generation of SMEs. Flow disturbances caused by topographic obstacles, including capes, islands, seamounts, etc., lead to eddy generation (Gula et al., 2015, 2016; Rubio et al., 2018). Isoguchi et al. (2009) elaborated on the consequence that eddies induced by the interaction between the strong Kuroshio Current and island topography. The topography hindered the movement of flow, causing flow separation and fur-

ther forming eddies.

Figure 11 shows an example of the SME located behind a cape (Fig. 7b black box), where eddies detected in this paper are frequently observed. The evolution of the SME generation near the cape was tracked via its SSTA signature since March 1, 2014, solstice 4 (Figs 11a, b, d, e). Figure 11c shows the background flow field and SLA contour on March 1, 2014. The Kuroshio Current impacted the cape from the southwest at a speed of 30–40 km, and the current experienced a slight disturbance and separation. We suspect that the eddy was generated by the interaction of current and topographic obstacles. Analyzing the SSTA images, the coastal temperature to the north of the cape gradually decreased as the KC pressed on the coast, and cold water gradually spread to the far sea (Figs 11a, b, d, e). As the KC impacted, the contour line protruded (Fig. 11b). The cold eddy (36.2°N, 141.3°E) whose diameter was approximately 20 km was well pronounced to the northeast of the cape. The core of the eddy was approximately 0.6°C colder than the surrounding waters. Figure 11f displays the geographic distribution of chlorophyll *a* concentration identical to that of the SSTA field on March 4, 2014, where the chlorophyll concentration (approximately 0.3 mg/m^3) was higher than that of the surrounding seawater. This could have been caused by two factors: the eddy captured water rich in chlorophyll from the coast to the sea, or the vertical nutrient transfer of the eddy. Furthermore, observing the transfer of chlorophyll concentration in space, a spiral arm around the eddy could be observed, which indicated the formation track and rotating sense of the eddy. The water mass carried chlorophyll from the coast to the northeast, and the rotating direction was counterclockwise, which was coincident with a cold eddy (cyclone). Therefore, it is significant that there was the generation of the eddy in the flow instability due to the interaction of topographic obstacles and current.

4.4 *Eddy formation due to atmospheric forcing*

Atmospheric forcing plays an obvious role in the generation of smaller mesoscale eddies, and the wind is an important factor in modulating the dynamic processes of the Kuroshio Extension (Jia et al., 2019; Shan et al., 2020). An increasing wind curl corresponds with energetic eddy activities and induces the intensive formation of mesoscale cyclones (He et al., 2017; Kubryakov and Stanichny, 2015).

In the KE region, according to the fusion eddy detection algorithm, a cold eddy was captured on January 4, 2014 (Figs 12 and 13), whose generation might have related to wind. Figure 12 upper panels show the local flow field and sea level anomaly around the eddy from January 3 to 5, 2014. There was a meandering flow in the middle of the SLA maps (33.5°N, 163.3°E). The current was stable, and its strength and direction remained almost unchanged, with a velocity of approximately 50 cm/s. Figure 12 lower panels show the local SSTA maps simultaneously, which show that the seawater moved gradually, forming a relatively balanced water mass on January 5, 2014, that is, the observed cold eddy. According to the detection and SSTA maps, the eddy size was approximately 25–30 km, and the temperature difference between the center and periphery of the eddy was approximately 1–1.5°C. During the evolution of the eddy, an image of chlorophyll a concentration is shown in Fig. 13a. Unfortunately, it was partially covered by clouds, but it can still be observed that there was an area rich in Chl, which corresponded to the position of the SSTA. The chlorophyll concentration in the eddy center was approximately higher than 0.25 mg/m^3, which indicated the vertical movement of the eddy. The spatial distribution of the wind stress curl shows in Figs 13b and c. An increasing wind stress curl enhances the generation of cyclones associated with cold anomalies, whereas a decrease in the wind stress curl strengthens anti-

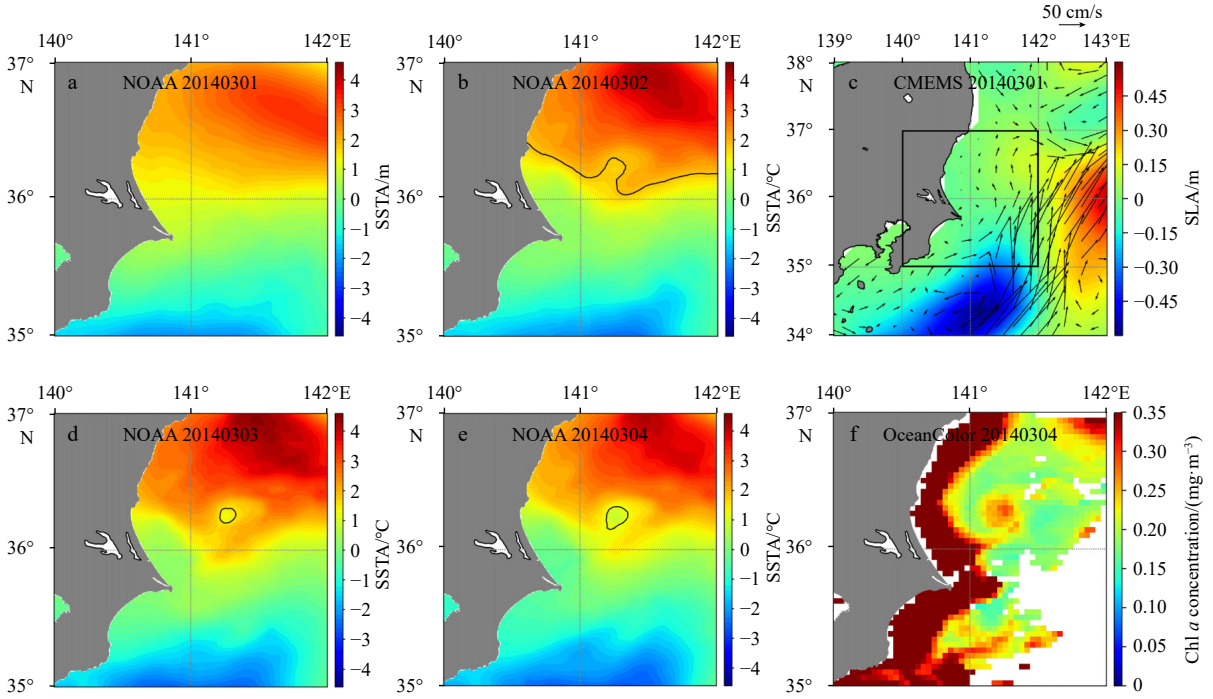

Fig. 11. Observed sea surface temperature snapshots from NOAA data: the color background represents the sea surface temperature anomaly (SSTA), the black line and circles (derived from NOAA) manifest the location of the smaller mesoscale eddy (SME) (a, b, d, and e); enlarged sea level anomaly (SLA) field superimposed velocity derived from Copernicus Marine Environment Monitoring Service data, the color represents SLA and the arrows represent current vectors (c); observed chlorophyll *a* concentration snapshot on March 4, 2014 (f).

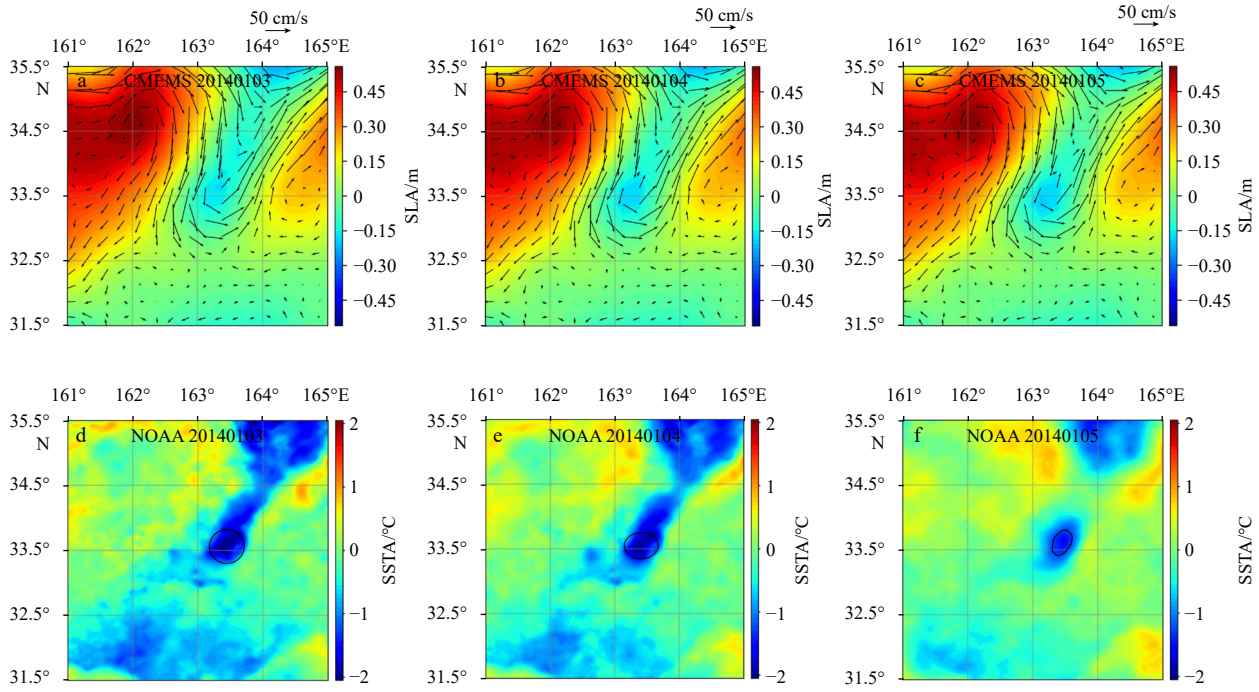

Fig. 12. Sea level anomaly (SLA) field (colors) superimposed current velocity from Copernicus Marine Environment Monitoring Service data (black arrows, derived from Absolute Dynamic Topography) (a–c); sea surface temperature anomaly (SSTA) fields from NOAA (d–f). The black circles represent the locations of the smaller mesoscale eddies.

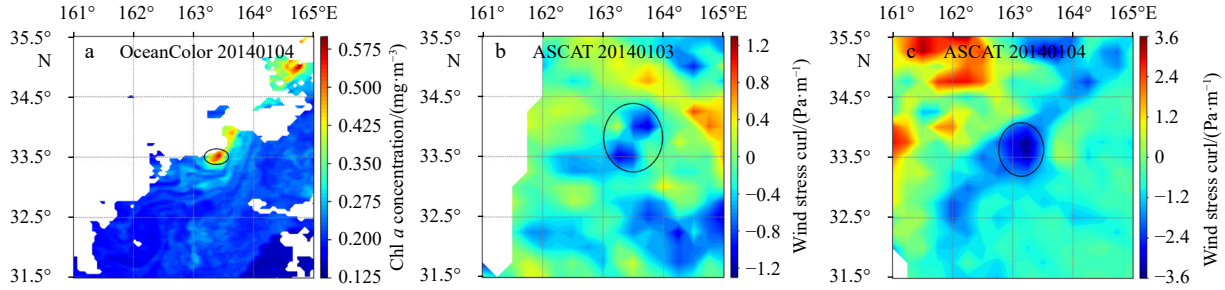

Fig. 13. Chlorophyll *a* concentration map from OceanColor (a), wind stress curl distribution from Advanced Scatterometer (b, c). The black circles represent the locations of the smaller mesoscale eddies.

cyclonic eddies associated with warm anomalies (Frenger et al., 2013; Kubryakov and Stanichny, 2015). There was also a strong wind stress curl in the position of cold eddy generation, which is consistent with the previous conclusion. This suggests that the wind stress curl is a reason for eddy generation. Considering the wind field, flow field, and terrain comprehensively, the current velocity was relatively stable, and there was no topographic obstacle at the eddy location. According to the ASCAT data, the intense wind stress curl weakened and disappeared gradually after January 4. After the intense wind stress curl, the eddy was absent on the SSTA maps. This fact suggests that the wind stress curl was possibly significant for eddy genesis.

5 Discussion and conclusions

Microwave remote sensing is entering a platform stage in the field of eddy observation. Infrared remote sensing and ocean color remote sensing instead of traditional altimeters provide potential feasibility to characterize SMEs because of their advantage of high accuracy and resolution. A detection algorithm that allows identifying eddies on the base of satellite SST and Chl data is presented. Eddies are extracted depending on their characteristics in the temporal and spatial distribution of SST and Chl anomaly. The algorithm was applied to a high-eddy-activity zone, the Kuroshio Extension. Further, the distribution and generation of SMEs in the KE were observed and analyzed by combining altimetry, drifter, and wind data.

The distribution of SMEs shows obvious seasonal variations, and the SMEs tend to be distributed on both sides of the KC spindle. Three types of SME formation are successfully observed based on the eddy detection method. Typical examples are shown in the previous section. According to observations, SMEs always form on the edge of mesoscale eddies due to horizontal strain instability, mainly located near the meandering current of the KC. SMEs are always encountered on the Japanese coast, restricted by the geographic distribution. Atmospheric forces, especially wind, maybe important influencing factors causing the formation of SMEs.

The algorithm is capable of providing a method for SME identification, and it also has weaknesses. The weight coefficient between SST and Chl in the algorithm needs to be further studied by exploring the quantitative effects of SST and Chl on SMEs or optimizing by deep learning. Moreover, a strict assessment

condition is established to identify eddies as accurately as possible, which might prevent some eddies from being observed. Ideally, the ultimate goal is to identify all oceanic eddies with satisfactory accuracy. In reality, it can never be realized but can gradually be approached. With the advent of ocean radar satellites, upcoming wide-swath interferometric altimeters (such as "SWOT", Surface Water and Ocean Topography, and "Guanlan") will hopefully characterize the sea surface height at smaller scales that have never been resolved before (Chen et al., 2019; Durand et al., 2010). In the future, we hope to couple the new-generation interferometric altimeters to optimize the detection algorithm and realize more accurate observations of smaller mesoscale eddies.

References

Abhishek P, Sil S. 2019. Validation of multi-scale ultra-high resolution (MUR) sea surface temperature with coastal buoys observations and applications for coastal fronts in the Bay of Bengal. In: Proceedings of 2019 URSI Asia-Pacific Radio Science Conference (AP-RASC). New Delhi, India: IEEE

Alpers W, Brandt P, Lazar A, et al. 2013. A small-scale oceanic eddy off the coast of West Africa studied by multi-sensor satellite and surface drifter data. Remote Sensing of Environment, 129: 132–143, doi: 10.1016/j.rse.2012.10.032

Capet X, McWilliams J C, Molemaker M J, et al. 2008. Mesoscale to submesoscale transition in the California current system. Part I: flow structure, eddy flux, and observational tests. Journal of Physical Oceanography, 38(1): 29–43, doi: 10.1175/2007JPO3671.1

Chelton D B, Gaube P, Schlax M G, et al. 2011. The influence of nonlinear mesoscale eddies on near-surface oceanic chlorophyll. Science, 334(6054): 328–332, doi: 10.1126/science.1208897

Chen Ge, Tang Junwu, Zhao Chaofang, et al. 2019. Concept design of the "Guanlan" science mission: China's novel contribution to space oceanography. Frontiers in Marine Science, 6: 194, doi: 10.3389/fmars.2019.00194

Chen Baiyang, Xie Lingling, Zheng Quanan, et al. 2020. Seasonal variability of mesoscale eddies in the Banda Sea inferred from altimeter data. Acta Oceanologica Sinica, 39(12): 11–20, doi: 10.1007/s13131-020-1665-2

Dandapat S, Chakraborty A. 2016. Mesoscale eddies in the western Bay of Bengal as observed from satellite altimetry in 1993–2014: statistical characteristics, variability and three-dimensional properties. IEEE Journal of Selected Topics in Applied Earth Observations and Remote Sensing, 9(11): 5044–5054, doi: 10.1109/JSTARS.2016.2585179

Dong Changming, Nencioli F, Liu Yu, et al. 2011. An automated approach to detect oceanic eddies from satellite remotely sensed sea surface temperature data. IEEE Geoscience and Remote Sensing Letters, 8(6): 1055–1059, doi: 10.1109/LGRS.2011.2155029

Durand M, Fu Lee-Lueng, Lettenmaier D P, et al. 2010. The surface water and ocean topography mission: observing terrestrial surface water and oceanic submesoscale eddies. Proceedings of the IEEE, 98(5): 766–779, doi: 10.1109/JPROC.2010.2043031

Frenger I, Gruber N, Knutti R, et al. 2013. Imprint of Southern Ocean eddies on winds, clouds and rainfall. Nature Geoscience, 6(8): 608–612, doi: 10.1038/ngeo1863

Fu Lee Lueng, Le Traon P Y. 2006. Satellite altimetry and ocean dynamics. Comptes Rendus Geoscience, 338(14–15): 1063–1076, doi: 10.1016/j.crte.2006.05.015

Gaultier L, Ubelmann C, Fu Lee-Lueng. 2016. The challenge of using future SWOT data for oceanic field reconstruction. Journal of Atmospheric and Oceanic Technology, 33(1): 119–126, doi: 10.1175/JTECH-D-15-0160.1

Gula J, Molemaker M J, McWilliams J C. 2015. Topographic vorticity generation, submesoscale instability and vortex street formation in the Gulf Stream. Geophysical Research Letters, 42(10): 4054–4062, doi: 10.1002/2015GL063731

Gula J, Molemaker M J, McWilliams J C. 2016. Topographic generation of submesoscale centrifugal instability and energy dissipation. Nature Communications, 7(1): 12811, doi: 10.1038/ncomms12811

Hansen D V, Poulain P M. 1996. Quality control and interpolations of WOCE-TOGA drifter data. Journal of Atmospheric and Oceanic Technology, 13(4): 900–909, doi: 10.1175/1520-0426(1996)013<0900:QCAIOW>2.0.CO;2

He Yinghui, Feng Ming, Xie Jieshuo, et al. 2017. Spatiotemporal variations of mesoscale eddies in the Sulu Sea. Journal of Geophysical Research: Oceans, 122(10): 7867–7879, doi: 10.1002/2017JC013153

Hsu P C, Ho C Y, Lee H J, et al. 2020. Temporal variation and spatial structure of the Kuroshio-induced submesoscale island vortices observed from GCOM-C and Himawari-8 data. Remote Sensing, 12(5): 883, doi: 10.3390/rs12050883

Hu Chuanmin, Lee Zhongping, Franz B. 2012. Chlorophyll *a* algorithms for oligotrophic oceans: a novel approach based on three-band reflectance difference. Journal of Geophysical Research: Oceans, 117(C1): C01011

Huang Xueping, Zhou Xinhua, Wang Zhiqiang, et al. 2012. CD99 triggers upregulation of mir-9-modulated PRDM1/BLIMP1 in Hodgkin/Reed-Sternberg cells and induces redifferentiation. International Journal of Cancer, 131(4): E382–E394, doi: 10.1002/ijc.26503

Isoguchi O, Shimada M, Sakaida F, et al. 2009. Investigation of Kuroshio-induced cold-core eddy trains in the lee of the Izu islands using high-resolution satellite images and numerical simulations. Remote Sensing of Environment, 113(9): 1912–1925, doi: 10.1016/j.rse.2009.04.017

Ji Jinlin, Dong Changming, Zhang Biao, et al. 2018. Oceanic eddy characteristics and generation mechanisms in the Kuroshio Extension region. Journal of Geophysical Research: Oceans, 123(11): 8548–8567, doi: 10.1029/2018JC014196

Jia Yinglai, Chen Longjing, Liu Qinyu, et al. 2019. The role of background wind and moisture in the atmospheric response to oceanic eddies during winter in the Kuroshio Extension region. Atmosphere, 10(9): 5279

Klein P, Lapeyre G. 2009. The oceanic vertical pump induced by mesoscale and submesoscale turbulence. Annual Review of Marine Science, 1: 351–375, doi: 10.1146/annurev.marine.010908.163704

Kubryakov A A, Stanichny S V. 2015. Seasonal and interannual variability of the black sea eddies and its dependence on characteristics of the large-scale circulation. Deep-Sea Research Part I: Oceanographic Research Papers, 97: 80–91, doi: 10.1016/j.dsr.2014.12.002

Li Jianing, Dong Jihai, Yang Qingxuan, et al. 2019a. Spatial-temporal variability of submesoscale currents in the South China Sea. Journal of Oceanology and Limnology, 37(2): 474–485, doi: 10.1007/s00343-019-8077-1

Li Jitao, Liang Yongquan, Zhang Jie, et al. 2019b. A new automatic oceanic mesoscale eddy detection method using satellite altimeter data based on density clustering. Acta Oceanologica Sinica, 38(5): 134–141, doi: 10.1007/s13131-019-1447-x

Li Yuheng, Sun Weifu, Zhang Jie, et al. 2021. Reconstruction of arctic SST data and generation of multi-source satellite fusion products with high temporal and spatial resolutions. Remote Sensing Letters, 12(7): 695–703, doi: 10.1080/2150704X.2021.1931531

Luo Shihao, Jing Zhiyou, Qi Yiquan. 2020. Submesoscale flows associated with convergent strain in an anticyclonic eddy of the Kuroshio Extension: a high-resolution numerical study. Ocean Science Journal, 55(2): 249–264, doi: 10.1007/s12601-020-0022-x

McGillicuddy Jr D J. 2016. Mechanisms of physical-biological-biogeochemical interaction at the oceanic mesoscale. Annual Review of Marine Science, 8: 125–159, doi: 10.1146/annurev-marine-010814-015606

McWilliams J C, Colas F, Molemaker M J. 2009. Cold filamentary intensification and oceanic surface convergence lines. Geophysical Research Letters, 36(18): L18602, doi: 10.1029/2009GL

039402
Munk W. 2001. Spirals on the sea. Scientia Marina, 65(S2): 193–198, doi: 10.3989/scimar.2001.65s2193
Nencioli F, Dong Changming, Dickey T, et al. 2010. A vector geometry-based eddy detection algorithm and its application to a high-resolution numerical model product and high-frequency radar surface velocities in the Southern California Bight. Journal of Atmospheric and Oceanic Technology, 27(3): 564–579, doi: 10.1175/2009JTECHO725.1
Qian Sijia, Yu Fangjie, Chen Ge. 2021. Distribution characteristics of eddies with a scale of 50~100 km in the Kuroshio Extension Region. Marine Sciences, 45(11): 10–19
Qiu Bo, Chen Shuiming. 2005. Eddy-induced heat transport in the subtropical North Pacific from Argo, TMI, and altimetry measurements. Journal of Physical Oceanography, 35(4): 458–473, doi: 10.1175/JPO2696.1
Qiu Bo, Chen Shuiming. 2010. Eddy-mean flow interaction in the decadally modulating Kuroshio Extension system. Deep-Sea Research Part II: Topical Studies in Oceanography, 57(13–14): 1098–1110, doi: 10.1016/j.dsr2.2008.11.036
Qiu Bo, Kelly K A, Joyce T M. 1991. Mean flow and variability in the Kuroshio Extension from Geosat altimetry data. Journal of Geophysical Research: Oceans, 96(C10): 18491–18507, doi: 10.1029/91JC01834
Rubio A, Caballero A, Orfila A, et al. 2018. Eddy-induced cross-shelf export of high Chl-a coastal waters in the SE Bay of Biscay. Remote Sensing of Environment, 205: 290–304, doi: 10.1016/j.rse.2017.10.037
Sasai Y, Richards K J, Ishida A, et al. 2010. Effects of cyclonic mesoscale eddies on the marine ecosystem in the Kuroshio Extension region using an eddy-resolving coupled physical-biological model. Ocean Dynamics, 60(3): 693–704, doi: 10.1007/s10236-010-0264-8
Sasaki H, Klein P, Qiu Bo, et al. 2014. Impact of oceanic-scale interactions on the seasonal modulation of ocean dynamics by the atmosphere. Nature Communications, 5(1): 5636, doi: 10.1038/ncomms6636
Shafeeque M, Balchand A N, Shah P, et al. 2021. Spatio-temporal variability of chlorophyll-*a* in response to coastal upwelling and mesoscale eddies in the South Eastern Arabian Sea. International Journal of Remote Sensing, 42(13): 4840–4867
Shan Xuan, Jing Zhao, Sun Bingrong, et al. 2020. Impacts of ocean current-atmosphere interactions on mesoscale eddy energetics in the Kuroshio Extension region. Geoscience Letters, 7(1): 3, doi: 10.1186/s40562-020-00152-w
Su Zhan, Wang Jinbo, Klein P, et al. 2018. Ocean submesoscales as a key component of the global heat budget. Nature Communications, 9: 775, doi: 10.1038/s41467-018-02983-w
Sun Shuangwen, Fang Yue, Liu Baochao, et al. 2016. Coupling between SST and wind speed over mesoscale eddies in the South China Sea. Ocean Dynamics, 66(11): 1467–1474, doi: 10.1007/s10236-016-0993-4
Taburet G, Sanchez-Roman A, Ballarotta M, et al. 2019. DUACS DT2018: 25 years of reprocessed sea level altimetry products. Ocean Science, 15(5): 1207–1224, doi: 10.5194/os-15-1207-2019
Tedesco P, Gula J, Ménesguen C, et al. 2019. Generation of submesoscale frontal eddies in the Agulhas current. Journal of Geophysical Research: Oceans, 124(11): 7606–7625, doi: 10.1029/2019JC015229
Trott C B, Subrahmanyam B, Nyadjro E S. 2019. Influence of mesoscale features on mixed layer dynamics in the Arabian Sea. Journal of Geophysical Research: Oceans, 124(5): 3361–3377, doi: 10.1029/2019JC014965
Uchiyama Y, Suzue Y, Yamazaki H. 2017. Eddy-driven nutrient transport and associated upper-ocean primary production along the Kuroshio. Journal of Geophysical Research: Oceans, 122(6): 5046–5062, doi: 10.1002/2017JC012847
Wang Jiahao, Mao Kefeng, Chen Xi, et al. 2020. Evolution and structure of the Kuroshio Extension front in spring 2019. Journal of Marine Science and Engineering, 8(7): 502, doi: 10.3390/jmse8070502
Williams R G. 2011. Ocean eddies and plankton blooms. Nature Geoscience, 4(11): 739–740, doi: 10.1038/ngeo1307
Yang Yang, San Liang X. 2018. On the seasonal eddy variability in the Kuroshio Extension. Journal of Physical Oceanography, 48(8): 1675–1689, doi: 10.1175/JPO-D-18-0058.1
Yang Xiao, Xu Guangjun, Liu Yu, et al. 2020. Multi-source data analysis of mesoscale eddies and their effects on surface chlorophyll in the bay of Bengal. Remote Sensing, 12(21): 3485, doi: 10.3390/rs12213485
Yasuda I, Okuda K, Hirai M. 1992. Evolution of a Kuroshio warm-core ring-variability of the hydrographic structure. Deep-Sea Research Part A. Oceanographic Research Papers, 39(S1): S131–S161
Zatsepin A, Kubryakov A, Aleskerova A, et al. 2019. Physical mechanisms of submesoscale eddies generation: evidences from laboratory modeling and satellite data in the Black Sea. Ocean Dynamics, 69(2): 253–266, doi: 10.1007/s10236-018-1239-4
Zhang Yingjun, Hu Chuanmin, Liu Yonggang, et al. 2019a. Submesoscale and mesoscale eddies in the Florida Straits: observations from satellite ocean color measurements. Geophysical Research Letters, 46(22): 13262–13270, doi: 10.1029/2019GL083999
Zhang Zhengguang, Qiu Bo. 2018. Evolution of submesoscale ageostrophic motions through the life cycle of oceanic mesoscale eddies. Geophysical Research Letters, 45(21): 11847–11855, doi: 10.1029/2018GL080399
Zhang Zhengguang, Qiu Bo. 2020. Surface chlorophyll enhancement in mesoscale eddies by submesoscale spiral bands. Geophysical Research Letters, 47(14): e2020GL088820
Zhang Zhengguang, Qiu Bo, Klein P, et al. 2019b. The influence of geostrophic strain on oceanic ageostrophic motion and surface chlorophyll. Nature Communications, 10(1): 2838, doi: 10.1038/s41467-019-10883-w
Zhang Zhiwei, Tian Jiwei, Qiu Bo, et al. 2016. Observed 3D structure, generation, and dissipation of oceanic mesoscale eddies in the South China Sea. Scientific Reports, 6: 24349, doi: 10.1038/srep24349
Zhang Chunhua, Xi Xiaoliang, Liu Songtao, et al. 2014. A mesoscale eddy detection method of specific intensity and scale from SSH image in the South China Sea and the Northwest Pacific. Science China Earth Sciences, 57(8): 1897–1906, doi: 10.1007/s11430-014-4839-y
Zhang Zhiwei, Zhang Yuchen, Qiu Bo, et al. 2020. Spatiotemporal characteristics and generation mechanisms of submesoscale currents in the northeastern South China Sea revealed by numerical simulations. Journal of Geophysical Research: Oceans, 125(2): e2019JC015404
Zheng Shaojun, Du Yan, Li Jiaxun, et al. 2015. Eddy characteristics in the South Indian Ocean as inferred from surface drifters. Ocean Science, 11(3): 361–371, doi: 10.5194/os-11-361-2015